

# BASNet: Boundary-Aware Salient Object Detection

Xuebin Qin, Zichen Zhang, Chenyang Huang, Chao Gao, Masood Dehghan and Martin Jagersand  
University of Alberta, Canada

{xuebin, vincent.zhang, chuang8, cgao3, masood1, mj7}@ualberta.ca

## Abstract

Deep Convolutional Neural Networks have been adopted for salient object detection and achieved the state-of-the-art performance. Most of the previous works however focus on region accuracy but not on the boundary quality. In this paper, we propose a predict-refine architecture, BASNet, and a new hybrid loss for Boundary-Aware Salient object detection. Specifically, the architecture is composed of a densely supervised Encoder-Decoder network and a residual refinement module, which are respectively in charge of saliency prediction and saliency map refinement. The hybrid loss guides the network to learn the transformation between the input image and the ground truth in a three-level hierarchy – pixel-, patch- and map- level – by fusing Binary Cross Entropy (BCE), Structural SIMilarity (SSIM) and Intersection-over-Union (IoU) losses. Equipped with the hybrid loss, the proposed predict-refine architecture is able to effectively segment the salient object regions and accurately predict the fine structures with clear boundaries. Experimental results on six public datasets show that our method outperforms the state-of-the-art methods both in terms of regional and boundary evaluation measures. Our method runs at over 25 fps on a single GPU. The code is available at: <https://github.com/NathanUA/BASNet>.

## 1. Introduction

The human vision system has an effective attention mechanism for choosing the most important information from visual scenes. Computer vision aims at modeling this mechanism in two research branches: eye-fixation detection [20] and salient object detection [3]. Our work focuses on the second branch and aims at accurately segmenting the pixels of salient objects in an input image. The results have immediate applications in e.g. image segmentation/editing [53, 25, 11, 54] and manipulation [24, 43], visual tracking [32, 52, 55] and user interface optimization [12].

Recently, Fully Convolutional Neural Networks (FCN) [63], have been adopted for salient object detection. Although these methods achieve significant results compared

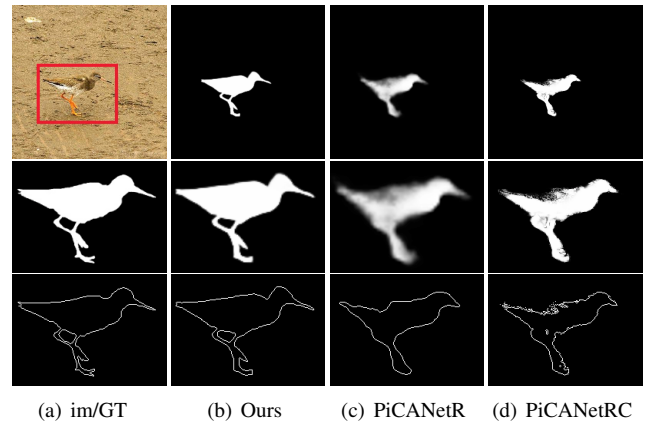


Figure 1. Sample result of our method (BASNet) compared to PiCANetR [39]. Column (a) shows the input image, zoom-in view of ground truth (GT) and the boundary map, respectively. (b), (c) and (d) are results of ours, PiCANetR and PiCANetRC (PiCANetR with CRF [27] post-processing). For each method, the three rows respectively show the predicted saliency map, the zoom-in view of saliency map and the zoom-in view of boundary map.

to traditional methods, their predicted saliency maps are still defective in fine structures and/or boundaries (see Figs. 1(c)-1(d)).

There are two main challenges in accurate salient object detection: (i) the saliency is mainly defined over the global contrast of the whole image rather than local or pixel-wise features. To achieve accurate results, the developed saliency detection methods have to understand the global meaning of the whole image as well as the detailed structures of the objects [6]. To address this problem, networks that aggregate multi-level deep features are needed; (ii) Most of the salient object detection methods use Cross Entropy (CE) as their training loss. But models trained with CE loss usually have low confidence in differentiating boundary pixels, leading to blurry boundaries. Other losses such as Intersection over Union (IoU) loss [56, 42, 47], F-measure loss [78] and Dice-score loss [8] were proposed for biased training sets but they are not specifically designed for capturing fine

structures.

To address the above challenges, we propose a novel Boundary-Aware network, namely **BASNet**, for Salient object detection, which achieves accurate salient object segmentation with high quality boundaries (see Fig. 1(b)): (i) To capture both global (coarse) and local (fine) contexts, a new predict-refine network is proposed. It assembles a U-Net-like [57] deeply supervised [31, 67] Encoder-Decoder network with a novel residual refinement module. The Encoder-Decoder network transfers the input image to a probability map, while the refinement module refines the predicted map by learning the residuals between the coarse saliency map and ground truth (see Fig. 2). In contrast to [50, 22, 6], which use refinement modules iteratively on saliency predictions or intermediate feature maps at multiple scales, our module is used only once on the original scale for saliency prediction. (ii) To obtain high confidence saliency map and clear boundary, we propose a hybrid loss that combines Binary Cross Entropy (BCE) [5], Structural SIMilarity (SSIM) [66] and IoU losses [42], which are expected to learn from ground truth information in pixel-, patch- and map- level, respectively. Rather than using explicit boundary losses (NLDF+ [41], C2S [36]), we implicitly inject the goal of accurate boundary prediction in the hybrid loss, contemplating that it may help reduce spurious error from cross propagating the information learned on the boundary and the other regions on the image.

The main contributions of this work are:

- A novel boundary-aware salient object detection network: BASNet, which consists of a deeply supervised encoder-decoder and a residual refinement module,
- A novel hybrid loss that fuses BCE, SSIM and IoU to supervise the training process of accurate salient object prediction on three levels: pixel-level, patch-level and map-level,
- A thorough evaluation of the proposed method that includes comparison with 15 state-of-the-art methods on six widely used public datasets. Our method achieves state-of-the-art results in terms of both regional and boundary evaluation measures.

## 2. Related Works

**Traditional Methods:** Early methods detect salient objects by searching for pixels according to a predefined saliency measure computed based on handcrafted features [69, 80, 60, 71]. Borji *et al.* provide a comprehensive survey in [3].

**Patch-wise Deep Methods:** Encouraged by the advancement on image classification of Deep CNNs [28, 59], early deep salient object detection methods search for salient objects by classifying image pixels or super pixels into salient or non-salient classes based on the lo-

cal image patches extracted from single or multiple scales [33, 40, 61, 79, 35]. These methods usually generate coarse outputs because spatial information are lost in the fully connected layers.

**FCN-based Methods:** Salient object detection methods based on FCN [34, 29] achieve significant improvement compared with patch-wise deep methods, presumably because FCN is able to capture richer spatial and multi-scale information. Zhang *et al.* (UCF) [75] developed a reformulated dropout and a hybrid upsampling module to reduce the checkboard artifacts of deconvolution operators as well as aggregating multi-level convolutional features in (Amulet) [74] for saliency detection. Hu *et al.* [18] proposed to learn a Level Set [48] function to output accurate boundaries and compact saliency. Luo *et al.* [41] designed a network (NLDF+) with a  $4 \times 5$  grid structure to combine local and global information and used a fusing loss of cross entropy and boundary IoU inspired by Mumford-Shah [46]. Hou *et al.* (DSS+) [17] adopted Holistically-Nested Edge Detector (HED) [67] by introducing short connections to its skip-layers for saliency prediction. Chen *et al.* (RAS) [4] adopted HED by refining its side-output iteratively using a reverse attention model. Zhang *et al.* (LFR) [73] predicted saliency with clear boundaries by proposing a sibling architecture and a structural loss function. Zhang *et al.* (BMPM) [72] proposed a controlled bi-directional passing of features between shallow and deep layers to obtain accurate predictions.

**Deep Recurrent and attention Methods:** Kuen *et al.* [30] proposed a recurrent network to iteratively perform refinement on selected image sub-regions. Zhang *et al.* (PA-GRN) [76] developed a recurrent saliency detection model that transfers global information from the deep layer to shallower layers by a multi-path recurrent connection. Hu *et al.* (RADF+) [19] recurrently concatenated multi-layer deep features for saliency object detection. Wang *et al.* (RFCN) [63] designed a recurrent FCN for saliency detection by iteratively correcting prediction errors. Liu *et al.* (PiCANetR) [39] predicted the pixel-wise attention maps by a contextual attention network and then incorporated it with U-Net architecture to detect salient objects.

**Coarse to Fine Deep Methods:** To capture finer structures and more accurate boundaries, numerous refinement strategies have been proposed. Liu *et al.* [38] proposed a deep hierarchical saliency network which learns various global structured saliency cues first and then progressively refine the details of saliency maps. Wang *et al.* (SRM) [64] proposed to capture global context information with a pyramid pooling module and a multi-stage refinement mechanism for saliency maps refinement. Inspired by [50], Amirul *et al.* [22] proposed an encoder-decoder network that utilizes a refinement unit to recurrently refine the saliency maps from low resolution to high resolution. Deng

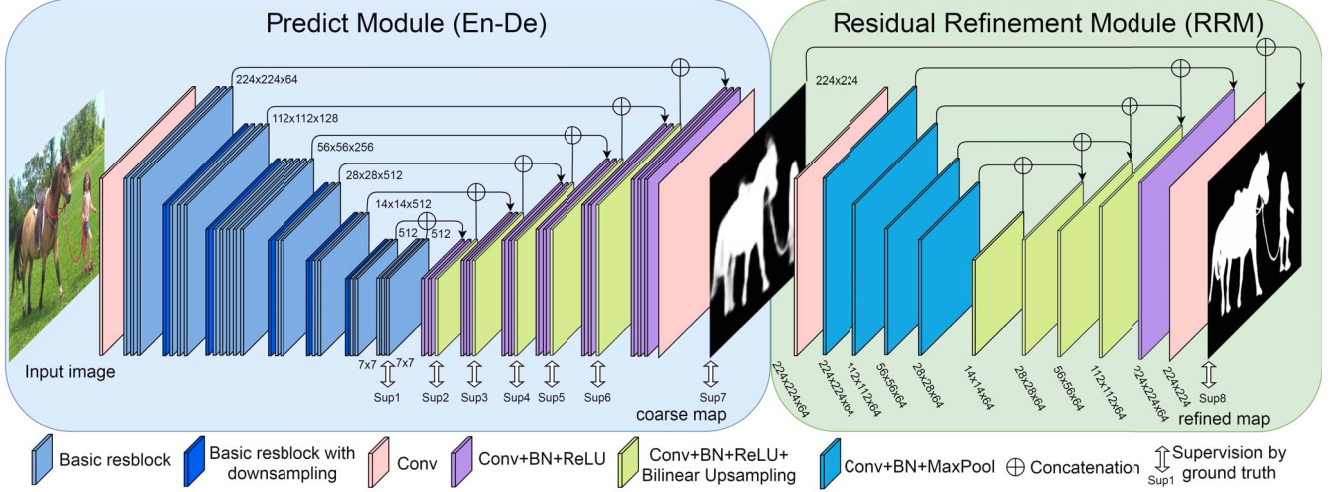


Figure 2. Architecture of our proposed boundary-aware salient object detection network: BASNet.

*et al.* (R<sup>3</sup>Net+) [6] developed a recurrent residual refinement network for saliency maps refinement by incorporating shallow and deep layers' features alternately. Wang *et al.* (DGRL) [65] proposed to localize salient objects globally and then refine them by a local boundary refinement module. Although these methods raise the bar of salient object detection greatly, there is still a large room for improvement in terms of the fine structure segment quality and boundary recovery accuracy.

### 3. BASNet

This section starts with the architecture overview of our proposed predict-refine model, BASNet. We describe the prediction module first in Sec. 3.2 followed by the details of our newly designed residual refinement module in Sec. 3.3. The formulation of our novel hybrid loss is presented in Sec. 3.4.

#### 3.1. Overview of Network Architecture

The proposed BASNet consists of two modules as shown in Fig. 2. The prediction module is a U-Net-like densely supervised Encoder-Decoder network [57], which learns to predict saliency map from input images. The multi-scale Residual Refinement Module (RRM) refines the resulting saliency map of the prediction module by learning the residuals between the saliency map and the ground truth.

#### 3.2. Predict Module

Inspired by U-Net [57] and SegNet [2], we design our salient object prediction module as an Encoder-Decoder network because this kind of architectures is able to capture high level global contexts and low level details at the same time. To reduce over fitting, the last layer of each decoder stage is supervised by the ground truth inspired by HED

[67] (see Fig. 2). The encoder part has an input convolution layer and six stages comprised of basic res-blocks. The input convolution layer and the first four stages are adopted from ResNet-34 [16]. The difference is that our input layer has 64 convolution filters with size of  $3 \times 3$  and stride of 1 rather than size of  $7 \times 7$  and stride of 2. Additionally, there is no pooling operation after the input layer. That means the feature maps before the second stage have the same spatial resolution as the input image. This is different from the original ResNet-34, which has quarter scale resolution in the first feature map. This adaptation enables the network to obtain higher resolution feature maps in earlier layers, while it also decreases the overall receptive fields. To achieve the same receptive field as ResNet-34 [16], we add two more stages after the fourth stage of ResNet-34. Both stages consist of three basic res-blocks with 512 filters after a non-overlapping max pooling layer of size 2.

To further capture global information, we add a bridge stage between the encoder and the decoder. It consists of three convolution layers with 512 dilated (dilation=2) [70]  $3 \times 3$  filters. Each of these convolution layers is followed by a batch normalization [21] and a ReLU activation function [13].

Our decoder is almost symmetrical to the encoder. Each stage consists of three convolution layers followed by a batch normalization and a ReLU activation function. The input of each stage is the concatenated feature maps of the upsampled output from its previous stage and its corresponding stage in the encoder. To achieve the side-output saliency maps, the multi-channel output of the bridge stage and each decoder stage is fed to a plain  $3 \times 3$  convolution layer followed by a bilinear upsampling and a sigmoid function. Therefore, given a input image, our predict module produces seven saliency maps in the training process. Al-

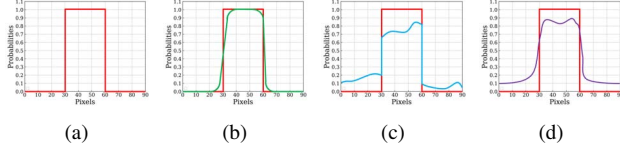


Figure 3. Illustration of different aspects of coarse prediction in one-dimension: (a) Red: probability plot of ground truth - GT, (b) Green: probability plot of coarse boundary not aligning with GT, (c) Blue: coarse region having too low probability, (d) Purple: real coarse predictions usually have both problems.

though every saliency map is upsampled to the same size with the input image, the last one has the highest accuracy and hence is taken as the final output of the predict module. This output is passed to the refinement module.

### 3.3. Refine Module

Refinement Module (RM) [22, 6] is usually designed as a residual block which refines the predicted coarse saliency maps  $S_{coarse}$  by learning the residuals  $S_{residual}$  between the saliency maps and the ground truth as

$$S_{refined} = S_{coarse} + S_{residual}. \quad (1)$$

Before introducing our refinement module, we have to define the term “coarse”. Here, “coarse” includes two aspects. One is the blurry and noisy boundaries (see its one-dimension (1D) illustration in Fig. 3(b)). The other one is the unevenly predicted regional probabilities (see Fig. 3(c)). The real predicted coarse saliency maps usually contain both coarse cases (see Fig. 3(d)).

Residual refinement module based on local context (RRM\_LC), Fig. 4(a), was originally proposed for boundary refinement [50]. Since its receptive field is small, Islam *et al.* [22] and Deng *et al.* [6] iteratively or recurrently use it for refining saliency maps on different scales. Wang *et al.* [64] adopted the pyramid pooling module from [15], in which three-scale pyramid pooling features are concatenated. To avoid losing details caused by pooling operations, RRM\_MS (Fig. 4(b)) uses convolutions with different kernel sizes and dilations [70, 72] to captures multi-scale contexts. However, these modules are shallow thus hard to capture high level information for refinement.

To refine both region and boundary drawbacks in coarse saliency maps, we develop a novel residual refinement module. Our RRM employs the residual encoder-decoder architecture, RRM\_Ours (see Figs. 2 and 4(c)). Its main architecture is similar but simpler to our predict module. It contains an input layer, an encoder, a bridge, a decoder and an output layer. Different from the predict module, both encoder and decoder have four stages. Each stage only has one convolu-

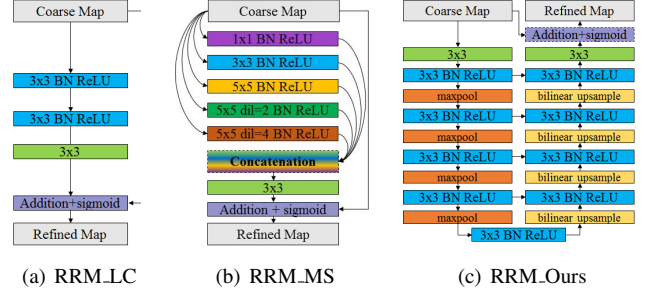


Figure 4. Illustration of different Residual Refine Modules (RRM): (a) local boundary refinement module RRM\_LC; (b) multi-scale refinement module RRM\_MS; (c) our encoder-decoder refinement module RRM\_Ours.

tion layer. Each layer has 64 filters of size  $3 \times 3$  followed by a batch normalization and a ReLU activation function. The bridge stage also has a convolution layer with 64 filters of size  $3 \times 3$  followed by a batch normalization and ReLU activation. Non-overlapping max pooling is used for down-sampling in the encoder and bilinear interpolation is utilized for the upsampling in the decoder. The output of this RM module is the final resulting saliency map of our model.

### 3.4. Hybrid Loss

Our training loss is defined as the summation over all outputs:

$$\mathcal{L} = \sum_{k=1}^K \alpha_k \ell^{(k)} \quad (2)$$

where  $\ell^{(k)}$  is the loss of the  $k$ -th side output,  $K$  denotes the total number of the outputs and  $\alpha_k$  is the weight of each loss. As described in Sec. 3.2 and Sec. 3.3, our salient object detection model is deeply supervised with eight outputs, i.e.  $K = 8$ , including seven outputs from the prediction model and one output from the refinement module.

To obtain high quality regional segmentation and clear boundaries, we propose to define  $\ell^{(k)}$  as a hybrid loss:

$$\ell^{(k)} = \ell_{bce}^{(k)} + \ell_{ssim}^{(k)} + \ell_{iou}^{(k)}. \quad (3)$$

where  $\ell_{bce}^{(k)}$ ,  $\ell_{ssim}^{(k)}$  and  $\ell_{iou}^{(k)}$  denote BCE loss [5], SSIM loss [66] and IoU loss [42], respectively.

BCE [5] loss is the most widely used loss in binary classification and segmentation. It is defined as:

$$\ell_{bce} = - \sum_{(r,c)} [G(r,c) \log(S(r,c)) + (1-G(r,c)) \log(1-S(r,c))] \quad (4)$$

where  $G(r, c) \in \{0, 1\}$  is the ground truth label of the pixel  $(r, c)$  and  $S(r, c)$  is the predicted probability of being salient object.

SSIM is originally proposed for image quality assessment [66]. It captures the structural information in an image. Hence, we integrated it into our training loss to learn



the structural information of the salient object ground truth. Let  $\mathbf{x} = \{x_j : j = 1, \dots, N^2\}$  and  $\mathbf{y} = \{y_j : j = 1, \dots, N^2\}$  be the pixel values of two corresponding patches (size:  $N \times N$ ) cropped from the predicted probability map  $S$  and the binary ground truth mask  $G$  respectively, the SSIM of  $\mathbf{x}$  and  $\mathbf{y}$  is defined as

$$\ell_{ssim} = 1 - \frac{(2\mu_x\mu_y + C_1)(2\sigma_{xy} + C_2)}{(\mu_x^2 + \mu_y^2 + C_1)(\sigma_x^2 + \sigma_y^2 + C_2)} \quad (5)$$

where  $\mu_x$ ,  $\mu_y$  and  $\sigma_x$ ,  $\sigma_y$  are the mean and standard deviations of  $\mathbf{x}$  and  $\mathbf{y}$  respectively,  $\sigma_{xy}$  is their covariance,  $C_1 = 0.01^2$  and  $C_2 = 0.03^2$  are used to avoid dividing by zero.

IoU is originally proposed for measuring the similarity of two sets [23] and then used as a standard evaluation measure for object detection and segmentation. Recently, it has been used as the training loss [56, 42]. To ensure its differentiability, we adopted the IoU loss used in [42]:

$$\ell_{iou} = 1 - \frac{\sum_{r=1}^H \sum_{c=1}^W S(r,c)G(r,c)}{\sum_{r=1}^H \sum_{c=1}^W [S(r,c) + G(r,c) - S(r,c)G(r,c)]} \quad (6)$$

where  $G(r, c) \in \{0, 1\}$  is the ground truth label of the pixel  $(r, c)$  and  $S(r, c)$  is the predicted probability of being salient object.

We illustrate the impact of each of the three losses in Fig. 5. These heatmaps show change of the loss at each pixel as the training progresses. The three rows correspond to the BCE loss, SSIM loss and IoU loss, respectively. The three columns represent different stages of the training process. BCE loss is pixel-wise. It does not consider the labels of the neighborhood and it weights both the foreground and background pixels equally. It helps with the convergence on all pixels.

SSIM loss is a patch-level measure, which considers a local neighborhood of each pixel. It assigns higher weights to the boundary, i.e., the loss is higher around the boundary, even when the predicted probabilities on the boundary and the rest of the foreground are the same. In the beginning of training, the loss along the boundary is the largest (see second row of Fig. 5). It helps the optimization to focus on the boundary. As the training progresses, the SSIM loss of the foreground reduces and the background loss becomes the dominant term. However, the background loss does not contribute to the training until when the prediction of background pixel becomes very close to the ground truth, where the loss drops rapidly from one to zero. This is helpful since the prediction typically goes close to zero only late in the training process where BCE loss becomes flat. The SSIM loss ensures that there's still enough gradient to drive the learning process. The background prediction looks cleaner since the probability is pushed to zero.

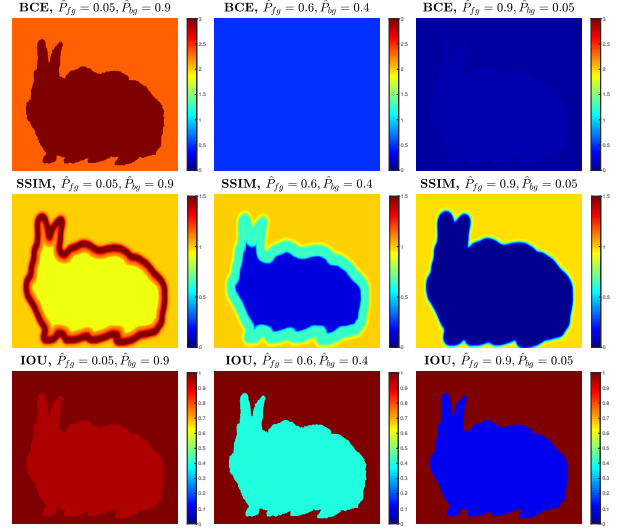


Figure 5. Illustration of the impact of the losses.  $\hat{P}_{fg}$  and  $\hat{P}_{bg}$  denote the predicted probability of the foreground and background, respectively.

IoU is a map-level measure. But we plot the per-pixel IoU following Eq. (6) for illustration purpose. As the confidence of the network prediction of the foreground grows, the loss of the foreground reduces eventually to zero. When combining these three losses, we utilize BCE to maintain a smooth gradient for all pixels, while using IoU to give more focus on the foreground. SSIM is used to encourage that the prediction respects the structure of the original image, by a larger loss near the boundary.

## 4. Experimental Results

### 4.1. Datasets

We evaluated our method on six frequently used benchmark datasets: SOD [45], ECSSD [68], DUT-OMRON [69], PASCAL-S [37], HKU-IS [33], DUTS [62]. **SOD** contains 300 images which are originally designed for image segmentation. These images are very challenging since most of them contains multiple salient objects either with low contrast or overlapping with the image boundary. **ECSSD** contains 1000 semantically meaningful but structurally complex images. **DUT-OMRON** has 5168 images with one or two objects in each images. Most of the foreground objects are structurally complex. **PASCAL-S** consists of 850 images with cluttered backgrounds and complex foreground objects. **HKU-IS** contains 4447 images. Most of them have more than one connected or disconnected foreground objects. **DUTS** is currently the largest saliency detection dataset. It is comprised of two subsets: DUTS-TR and DUTS-TE. **DUTS-TR** contains 10553 images designed for training and **DUTS-TE** has 5019 images for testing.

## 4.2. Implementation and Experimental Setup

We train our network using the DUTS-TR dataset, which has 10553 images. Before training, the dataset is augmented by horizontal flipping to 21106 images. During training, each image is first resized to  $256 \times 256$  and randomly cropped to  $224 \times 224$ . Part of the encoder parameters are initialized from the ResNet-34 model [16]. Other convolutional layers are initialized by Xavier [10]. We utilize the Adam optimizer [26] to train our network and its hyper parameters are set to the default values, where the initial learning rate  $lr=1e-3$ ,  $\beta_1=0.9$ ,  $\beta_2=0.999$ ,  $\epsilon=1e-8$ ,  $weight\_decay=0$ . We train the network until the loss converges without using validation set. The training loss converges after 400k iterations with a batch size of 8 and the whole training process takes about 125 hours. During testing, the input image is resized to  $256 \times 256$  and fed into the network to obtain its saliency map. Then, the saliency map ( $256 \times 256$ ) is resized back to the original size of the input image. Both the resizing processes use bilinear interpolation.

We implement our network based on the publicly available framework: Pytorch 0.4.0 [49]. An eight-core PC with an AMD Ryzen 1800x 3.5 GHz CPU (with 32GB RAM) and a GTX 1080ti GPU (with 11GB memory) is used for both training and testing. The inference for a  $256 \times 256$  image only takes 0.040s (**25 fps**). The source code will be released.

## 4.3. Evaluation Metrics

We use four measures to evaluate our method: Precision-Recall (PR) curve, F-measure, Mean Absolute Error (MAE) and relaxed F-measure of boundary ( $relaxF_\beta^b$ ).

PR curve is a standard way of evaluating the predicted saliency probability maps. The precision and recall of a saliency map are computed by comparing the binarized saliency map against the ground truth mask. Each binarizing threshold results in a pair of average precision and recall over all saliency maps in a dataset. Varying the threshold from 0 to 1 produces a sequence of precision-recall pairs, which is plotted as the PR curve.

Then, to have a comprehensive measure on both precision and recall,  $F_\beta$  is computed based on each pair of precision and recall as:

$$F_\beta = \frac{(1+\beta^2) \times Precision \times Recall}{\beta^2 \times Precision + Recall} \quad (7)$$

where  $\beta^2$  is set to 0.3 to weight precision more than recall [1]. The maximum  $F_\beta$  ( $maxF_\beta$ ) of each dataset is reported in this paper.

MAE [51] denotes the average absolute per-pixel difference between a predicted saliency map and its ground truth mask. Given a saliency map, its MAE is defined as:

$$MAE = \frac{1}{H \times W} \sum_{r=1}^H \sum_{c=1}^W |S(r, c) - G(r, c)| \quad (8)$$

Ablation	Configurations	$maxF_\beta$	$relaxF_\beta^b$	MAE
Architecture	Baseline U-Net [57] + $\ell_{bce}$	0.896	0.669	0.066
	En-De + $\ell_{bce}$	0.929	0.767	0.047
	En-De+Sup + $\ell_{bce}$	0.934	0.805	<b>0.040</b>
	En-De+Sup+RRM.LC + $\ell_{bce}$	0.936	0.803	<b>0.040</b>
	En-De+Sup+RRM.MS + $\ell_{bce}$	0.935	0.804	0.042
	En-De+Sup+RRM.Ours + $\ell_{bce}$	<b>0.937</b>	<b>0.806</b>	0.042
Loss	En-De+Sup+RRM.Ours + $\ell_{ssim}$	0.924	0.808	0.042
	En-De+Sup+RRM.Ours + $\ell_{iou}$	0.933	0.795	0.039
	En-De+Sup+RRM.Ours + $\ell_{bs}$	0.940	0.815	0.040
	En-De+Sup+RRM.Ours + $\ell_{bi}$	0.940	0.813	0.038
	En-De+Sup+RRM.Ours + $\ell_{bsi}$	<b>0.942</b>	<b>0.826</b>	<b>0.037</b>

Table 1. Ablation study on different architectures and losses: En-De: Encoder-Decoder, Sup: side output supervision;  $\ell_{bi} = \ell_{bce} + \ell_{iou}$ ,  $\ell_{bs} = \ell_{bce} + \ell_{ssim}$ ,  $\ell_{bsi} = \ell_{bce} + \ell_{ssim} + \ell_{iou}$ .

where  $S$  and  $G$  are saliency probability map and its ground truth respectively,  $H$  and  $W$  represents the height and width of the saliency map and  $(r, c)$  denotes the pixel coordinates. For a dataset, its MAE is the average MAE of all the saliency maps.

Additionally, we adopt the relaxed F-measure  $relaxF_\beta^b$  [7] to quantitatively evaluate boundaries. Given a saliency map  $S$ , we first convert it to a binary mask  $S_{bw}$  using a threshold of 0.5. Then, we obtain the mask of its one pixel wide boundary by conducting an  $XOR(S_{bw}, S_{erd})$  operation where  $S_{erd}$  is the eroded binary mask [14] of  $S_{bw}$ . The same method is used to get the boundaries of ground truth mask. The relaxed boundary precision ( $relaxPrecision^b$ ) is then defined as the fraction of predicted boundary pixels within a range of  $\rho$  pixels from ground truth boundary pixels. The relaxed boundary recall ( $relaxRecall^b$ ) measures the fraction of ground truth boundary pixels that are within  $\rho$  pixels of predicted boundary pixels. In our experiments, we set the slack parameter  $\rho$  to 3 similar to the previous studies [44, 58, 77]. The relaxed boundary F-measure  $relaxF_\beta^b$  of each predicted saliency map is computed using equation (7), in which  $Precision$  and  $Recall$  are replaced by  $relaxPrecision^b$  and  $relaxRecall^b$ . For each dataset, we report its average  $relaxF_\beta^b$  of all predicted saliency maps.

## 4.4. Ablation Study

In this section, we validate the effectiveness of each key components used in our model. The ablation study contains two parts: architecture ablation and loss ablation. The ablation experiments are conducted on the ECSSD dataset.

**Architecture ablation:** To prove the effectiveness of our BASNet, we report the quantitative comparison results of our model against other related architectures. We take U-Net [57] as our baseline network. Then we start with our proposed Encoder-Decoder network and progressively extend it with densely side output supervision and different residual refinement modules including RRM.LC, RRM.MS

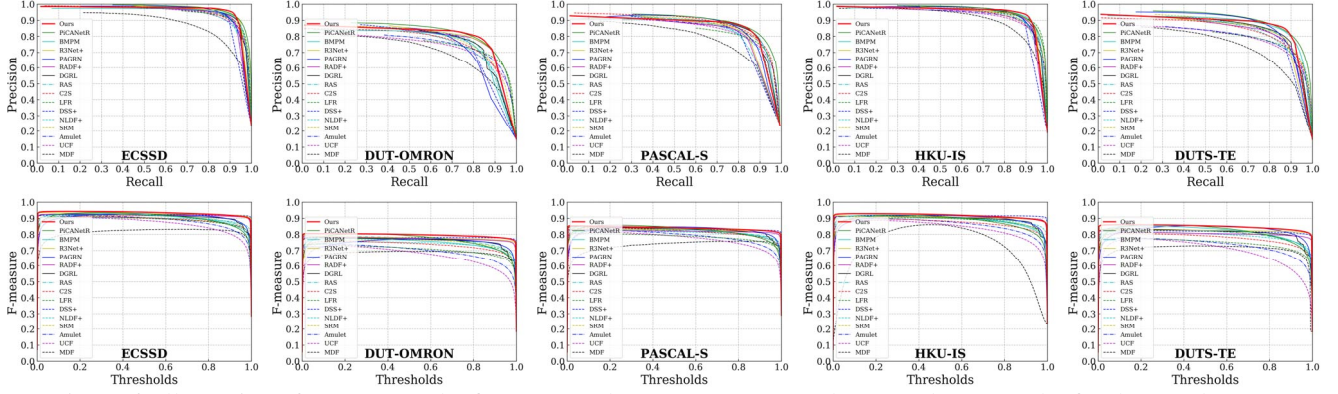


Figure 6. Illustration of PR curves (the first row) and F-measure curves (the second row) on the five largest dataset.

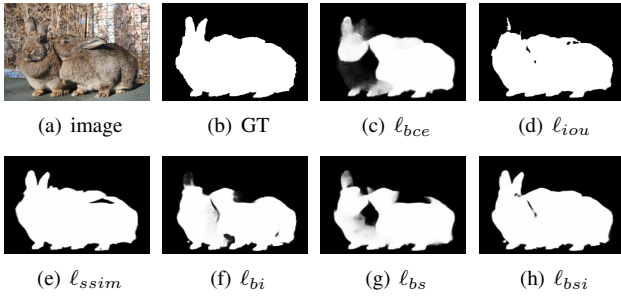


Figure 7. Sample results trained with our BASNet on different losses.

and RRM\_Ours. Table 1 illustrates the results of this ablation study. As we can see, our BASNet architecture achieves the best performance among these configurations.

**Loss ablation:** To demonstrate the effectiveness of our proposed fusion loss, we conduct a set of experiments over different losses based on our BASNet architecture. The results in Table 1 signifies that our proposed hybrid  $\ell_{bsi}$  loss greatly improves the performance, especially for the boundary quality. To further illustrate the qualitative effect of losses, results of our BASNet trained with different losses are shown in Fig. 7. It is clear that the proposed hybrid loss achieves superior qualitative results.

#### 4.5. Comparison with State-of-the-arts

We compare our method with 15 state-of-the-art models, PiCANetR [39], BMPM [72], R<sup>3</sup>Net [6], PAGRN [76], RADF [19], DGRL [65], RAS [4], C2S [36], LFR [73], DSS [17], NLDF [41], SRM [64], Amulet [74], UCF [75], MDF [35]. For fair comparison, we either use saliency maps provided by the authors or run their released models.

**Quantitative evaluation:** To evaluate the quality of segmented salient objects, we show the precision-recall curves (PR) and the F-measure curves for the five largest datasets in Fig. 6. In addition, Table 2 summarizes the maximum

region-based F-measure ( $\max F_\beta$ ), the relaxed boundary F-measure ( $\text{relax} F_\beta^b$ ) and the MAE measure for all datasets. As we can see, our method outperforms the state-of-the-arts in terms of both regional and boundary measures. Particularly, our method improves  $\text{relax} F_\beta^b$  by 4.1%, 5.1%, 6.2%, 6.2%, 3.4%, 5.9% on SOD, ECSSD, DUT-OMRON, PASCAL-S, HKU-IS and DUTS-TE datasets, respectively.

**Qualitative evaluation:** To further illustrate the superior performance of our method, Fig. 8 shows the qualitative comparison of the results with other top seven methods. We can see that our method is able to accurately segment salient objects under various challenging scenarios, including images with low contrast (1st and 2nd rows), fine structures (3rd and 4th rows), large object touching image boundaries (5th and 6th rows), complex object boundaries (7th and 8th rows), cluttered foreground and background (last two rows). We would like to emphasize that the saliency probability maps produced by our method (without CRF) are more uniform than that of others. In addition, the object boundaries of our results are more clear and sharper than others. More quantitative and qualitative comparison results are provided in the supplementary material.

## 5. Conclusion

In this paper, we proposed a novel end-to-end boundary-aware model, BASNet, and a hybrid fusing loss for accurate salient object detection. The proposed BASNet is a predict-refine architecture, which consists of two components: a prediction network and a refinement module. Combined with the hybrid loss, BASNet is able to capture both large-scale and fine structures, *e.g.* thin regions, holes, and produce salient object detection maps with clear boundaries. Experimental results on six datasets demonstrate that our model outperforms other 15 state-of-the-art methods in terms of both region-based and boundary-aware measures. Additionally, our proposed network architecture is modular. It can be easily extended or adapted to other tasks by replacing either the predicting network or the refinement module.

Table 2. Comparison of the proposed method and other 15 methods on six datasets in terms of the maximum F-measure  $maxF_{\beta}$  (larger is better), the relaxed boundary F-measure  $relaxF_{\beta}^b$  (larger is better) and the  $MAE$  (Smaller is better). **Red**, **Green**, and **Blue** indicate the best, second best and third best performance.”+” means the results are achieved with post-processing by CRF. “DT”, “MK”, “MB” are training dataset DUTS-TR, MSRA10K, MSRA-B respectively. “M30K” used in C2S is an extended dataset from MSRA10K.

Method	Backbone	Training data		SOD [45]			ECSSD [68]			DUT-OMRON [69]			PASCAL-S [37]			HKU-IS [33]			DUTS-TE [62]		
				$maxF_{\beta}$	$relaxF_{\beta}^b$	MAE	$maxF_{\beta}$	$relaxF_{\beta}^b$	MAE	$maxF_{\beta}$	$relaxF_{\beta}^b$	MAE	$maxF_{\beta}$	$relaxF_{\beta}^b$	MAE	$maxF_{\beta}$	$relaxF_{\beta}^b$	MAE	$maxF_{\beta}$	$relaxF_{\beta}^b$	MAE
Ours	ResNet-34	DT	10553	<b>0.851</b>	<b>0.603</b>	0.114	<b>0.942</b>	<b>0.826</b>	<b>0.037</b>	<b>0.805</b>	<b>0.694</b>	<b>0.056</b>	<b>0.854</b>	<b>0.660</b>	<b>0.076</b>	<b>0.928</b>	<b>0.807</b>	<b>0.032</b>	<b>0.860</b>	<b>0.758</b>	<b>0.047</b>
PiCANetR [39]	ResNet-50	DT	10553	<b>0.856</b>	0.528	<b>0.104</b>	<b>0.935</b>	<b>0.775</b>	0.046	<b>0.803</b>	<b>0.632</b>	0.065	<b>0.857</b>	<b>0.598</b>	<b>0.076</b>	<b>0.918</b>	<b>0.765</b>	0.043	<b>0.860</b>	<b>0.696</b>	<b>0.050</b>
BMPM [72]	VGG-16	DT	10553	<b>0.856</b>	<b>0.562</b>	<b>0.108</b>	0.928	<b>0.770</b>	0.045	0.774	<b>0.612</b>	0.064	<b>0.850</b>	<b>0.617</b>	<b>0.074</b>	<b>0.921</b>	<b>0.773</b>	0.039	0.852	<b>0.699</b>	<b>0.048</b>
R <sup>3</sup> Net+ [6]	ResNeXt	MK	10000	0.850	0.431	0.125	<b>0.934</b>	0.759	<b>0.040</b>	<b>0.795</b>	0.599	0.063	0.834	0.538	0.092	0.915	0.740	<b>0.036</b>	0.828	0.601	0.058
PAGRN [76]	VGG-19	DT	10553	-	-	-	0.927	0.747	0.061	0.771	0.582	0.071	0.847	0.594	0.0895	0.918	0.762	0.048	<b>0.854</b>	0.692	0.055
RADF+ [19]	VGG-16	MK	10000	0.838	0.476	0.126	0.923	0.720	0.049	0.791	0.579	<b>0.061</b>	0.830	0.515	0.097	0.914	0.725	0.039	0.821	0.608	0.061
DGRL [65]	ResNet-50	DT	10553	0.848	0.502	<b>0.106</b>	0.925	0.753	<b>0.042</b>	0.779	0.584	0.063	0.848	0.569	<b>0.074</b>	0.913	0.744	<b>0.037</b>	0.834	0.656	0.051
RAS [4]	VGG-16	MB	2500	0.851	<b>0.544</b>	0.124	0.921	0.741	0.056	0.786	0.615	<b>0.062</b>	0.829	0.560	0.101	0.913	0.748	0.045	0.831	0.656	0.059
C2S [36]	VGG-16	M30K	30000	0.823	0.457	0.124	0.910	0.708	0.055	0.758	0.565	0.072	0.840	0.543	0.082	0.896	0.717	0.048	0.807	0.607	0.062
LFR [3]	VGG-16	MK	10000	0.828	0.479	0.123	0.911	0.694	0.052	0.740	0.508	0.103	0.801	0.499	0.107	0.911	0.731	0.040	0.778	0.556	0.083
DSS+ [17]	VGG-16	MB	2500	0.846	0.444	0.124	0.921	0.696	0.052	0.781	0.559	0.063	0.831	0.499	0.093	0.916	0.706	0.040	0.825	0.606	0.056
NLDF+ [41]	VGG-16	MB	2500	0.841	0.475	0.125	0.905	0.666	0.063	0.753	0.514	0.080	0.822	0.495	0.098	0.902	0.694	0.048	0.813	0.591	0.065
SRM [64]	ResNet-50	DT	10553	0.843	0.392	0.128	0.917	0.672	0.054	0.769	0.523	0.069	0.838	0.509	0.084	0.906	0.680	0.046	0.826	0.592	0.058
Amulet [74]	VGG-16	MK	10000	0.798	0.454	0.144	0.915	0.711	0.059	0.743	0.528	0.098	0.828	0.541	0.100	0.897	0.716	0.051	0.778	0.568	0.084
UCF [75]	VGG-16	MK	10000	0.808	0.471	0.148	0.903	0.669	0.069	0.730	0.480	0.120	0.814	0.493	0.115	0.888	0.679	0.062	0.773	0.518	0.112
MDF [35]	R-CNN [9]	MB	2500	0.746	0.311	0.192	0.832	0.472	0.105	0.694	0.406	0.092	0.759	0.343	0.142	0.860	0.594	0.129	0.729	0.447	0.099

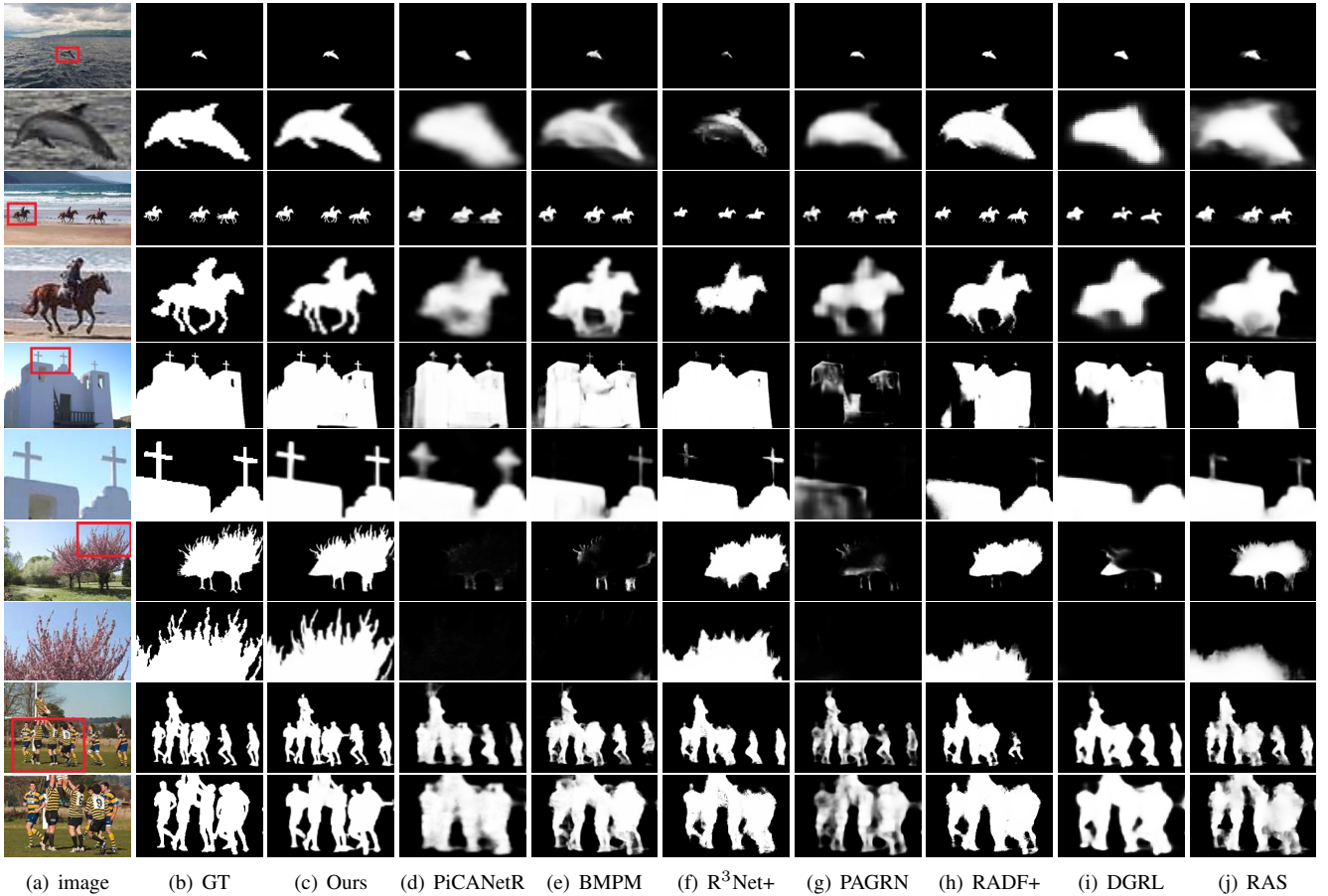


Figure 8. Qualitative comparison of the proposed method with seven other methods. Each sample occupies two rows. The second row of each sample is the zoom-in view.

**Acknowledgements.** This project was partially supported by Alberta Innovates Graduate Student Scholarship (AITF). We would like to thank Dr. Yiming Qian for his constructive

suggestions and Dr. Dana Cobzas for her GPU resources.



## References

- [1] Radhakrishna Achanta, Sheila Hemami, Francisco Estrada, and Sabine Susstrunk. Frequency-tuned salient region detection. In *Computer vision and pattern recognition, 2009. cvpr 2009. IEEE conference on*, pages 1597–1604. IEEE, 2009.
- [2] Vijay Badrinarayanan, Alex Kendall, and Roberto Cipolla. Segnet: A deep convolutional encoder-decoder architecture for image segmentation. *IEEE Transactions on Pattern Analysis & Machine Intelligence*, (12):2481–2495, 2017.
- [3] Ali Borji, Ming-Ming Cheng, Huaizu Jiang, and Jia Li. Salient object detection: A benchmark. *IEEE Trans. Image Processing*, 24(12):5706–5722, 2015.
- [4] Shuhan Chen, Xiuli Tan, Ben Wang, and Xuelong Hu. Reverse attention for salient object detection. In *Computer Vision - ECCV 2018 - 15th European Conference, Munich, Germany, September 8-14, 2018, Proceedings, Part IX*, pages 236–252, 2018.
- [5] Pieter-Tjerk de Boer, Dirk P. Kroese, Shie Mannor, and Reuven Y. Rubinstein. A tutorial on the cross-entropy method. *Annals OR*, 134(1):19–67, 2005.
- [6] Zijun Deng, Xiaowei Hu, Lei Zhu, Xuemiao Xu, Jing Qin, Guoqiang Han, and Pheng-Ann Heng. R3net: Recurrent residual refinement network for saliency detection. *IJCAI*, 2018.
- [7] Marc Ehrig and Jérôme Euzenat. Relaxed precision and recall for ontology matching. In *Proc. K-Cap 2005 workshop on Integrating ontology*, pages 25–32. No commercial editor., 2005.
- [8] Lucas Fidon, Wenqi Li, Luis C. Herrera, Jinendra Ekanayake, Neil Kitchen, Sébastien Ourselin, and Tom Vercauteren. Generalised wasserstein dice score for imbalanced multi-class segmentation using holistic convolutional networks. In *Brainlesion: Glioma, Multiple Sclerosis, Stroke and Traumatic Brain Injuries - Third International Workshop, BrainLes 2017, Held in Conjunction with MICCAI 2017, Quebec City, QC, Canada*, pages 64–76, 2017.
- [9] Ross Girshick, Jeff Donahue, Trevor Darrell, and Jitendra Malik. Rich feature hierarchies for accurate object detection and semantic segmentation. In *Proceedings of the IEEE conference on computer vision and pattern recognition*, pages 580–587, 2014.
- [10] Xavier Glorot and Yoshua Bengio. Understanding the difficulty of training deep feedforward neural networks. In *Proceedings of the Thirteenth International Conference on Artificial Intelligence and Statistics, AISTATS 2010, Chia Laguna Resort, Sardinia, Italy, May 13-15, 2010*, pages 249–256, 2010.
- [11] Stas Goferman, Lihi Zelnik-Manor, and Ayellet Tal. Context-aware saliency detection. *IEEE transactions on pattern analysis and machine intelligence*, 34(10):1915–1926, 2012.
- [12] Prakhar Gupta, Shubh Gupta, Ajaykrishnan Jayagopal, Sourav Pal, and Ritwik Sinha. Saliency prediction for mobile user interfaces. In *2018 IEEE Winter Conference on Applications of Computer Vision, WACV 2018, Lake Tahoe, NV, USA, March 12-15, 2018*, pages 1529–1538, 2018.
- [13] Richard HR Hahnloser and H Sebastian Seung. Permitted and forbidden sets in symmetric threshold-linear networks. In *Advances in Neural Information Processing Systems*, pages 217–223, 2001.
- [14] Robert M Haralick, Stanley R Sternberg, and Xinhua Zhuang. Image analysis using mathematical morphology. *IEEE transactions on pattern analysis and machine intelligence*, (4):532–550, 1987.
- [15] Kaiming He, Xiangyu Zhang, Shaoqing Ren, and Jian Sun. Spatial pyramid pooling in deep convolutional networks for visual recognition. In *European conference on computer vision*, pages 346–361. Springer, 2014.
- [16] Kaiming He, Xiangyu Zhang, Shaoqing Ren, and Jian Sun. Deep residual learning for image recognition. In *Proceedings of the IEEE conference on computer vision and pattern recognition*, pages 770–778, 2016.
- [17] Qibin Hou, Ming-Ming Cheng, Xiaowei Hu, Ali Borji, Zhuowen Tu, and Philip Torr. Deeply supervised salient object detection with short connections. In *2017 IEEE Conference on Computer Vision and Pattern Recognition (CVPR)*, pages 5300–5309. IEEE, 2017.
- [18] Ping Hu, Bing Shuai, Jun Liu, and Gang Wang. Deep level sets for salient object detection. In *CVPR*, volume 1, page 2, 2017.
- [19] Xiaowei Hu, Lei Zhu, Jing Qin, Chi-Wing Fu, and Pheng-Ann Heng. Recurrently aggregating deep features for salient object detection. In *Proceedings of AAAI-18, New Orleans, Louisiana, USA*, pages 6943–6950, 2018.
- [20] Xun Huang, Chengyao Shen, Xavier Boix, and Qi Zhao. Salicon: Reducing the semantic gap in saliency prediction by adapting deep neural networks. In *Proceedings of the IEEE International Conference on Computer Vision*, pages 262–270, 2015.
- [21] Sergey Ioffe and Christian Szegedy. Batch normalization: Accelerating deep network training by reducing internal covariate shift. *arXiv preprint arXiv:1502.03167*, 2015.
- [22] Md Amirul Islam, Mahmoud Kalash, Mrigank Roach, Neil DB Bruce, and Yang Wang. Salient object detection using a context-aware refinement network.
- [23] Paul Jaccard. The distribution of the flora in the alpine zone. 1. *New phytologist*, 11(2):37–50, 1912.
- [24] Martin Jägersand. Saliency maps and attention selection in scale and spatial coordinates: An information theoretic approach. In *ICCV*, pages 195–202, 1995.
- [25] Timor Kadir and Michael Brady. Saliency, scale and image description. *International Journal of Computer Vision*, 45(2):83–105, 2001.
- [26] Diederik P Kingma and Jimmy Ba. Adam: A method for stochastic optimization. *arXiv preprint arXiv:1412.6980*, 2014.
- [27] Philipp Krähenbühl and Vladlen Koltun. Efficient inference in fully connected crfs with gaussian edge potentials. In *Advances in neural information processing systems*, pages 109–117, 2011.
- [28] Alex Krizhevsky, Ilya Sutskever, and Geoffrey E. Hinton. Imagenet classification with deep convolutional neural networks. In *Advances in Neural Information Processing Systems 25: 26th Annual Conference on Neural Information*

- Processing Systems 2012. Proceedings of a meeting held December 3-6, 2012, Lake Tahoe, Nevada, United States.*, pages 1106–1114, 2012.
- [29] Srinivas SS Kruthiventi, Vennela Gudisa, Jaley H Dholakiya, and R Venkatesh Babu. Saliency unified: A deep architecture for simultaneous eye fixation prediction and salient object segmentation. In *Proceedings of the IEEE Conference on Computer Vision and Pattern Recognition*, pages 5781–5790, 2016.
  - [30] Jason Kuen, Zhenhua Wang, and Gang Wang. Recurrent attentional networks for saliency detection. In *Proceedings of the IEEE Conference on Computer Vision and Pattern Recognition*, pages 3668–3677, 2016.
  - [31] Chen-Yu Lee, Saining Xie, Patrick Gallagher, Zhengyou Zhang, and Zhuowen Tu. Deeply-supervised nets. In *Artificial Intelligence and Statistics*, pages 562–570, 2015.
  - [32] Hyemin Lee and Daijin Kim. Salient region-based online object tracking. In *2018 IEEE Winter Conference on Applications of Computer Vision, WACV 2018, Lake Tahoe, NV, USA, March 12-15, 2018*, pages 1170–1177, 2018.
  - [33] Guanbin Li and Yizhou Yu. Visual saliency based on multiscale deep features. In *Proceedings of the IEEE conference on computer vision and pattern recognition*, pages 5455–5463, 2015.
  - [34] Guanbin Li and Yizhou Yu. Deep contrast learning for salient object detection. In *Proceedings of the IEEE Conference on Computer Vision and Pattern Recognition*, pages 478–487, 2016.
  - [35] Guanbin Li and Yizhou Yu. Visual saliency detection based on multiscale deep cnn features. *IEEE Transactions on Image Processing*, 25(11):5012–5024, 2016.
  - [36] Xin Li, Fan Yang, Hong Cheng, Wei Liu, and Dinggang Shen. Contour knowledge transfer for salient object detection. In *Computer Vision - ECCV 2018 - 15th European Conference, Munich, Germany, September 8-14, 2018, Proceedings, Part XV*, pages 370–385, 2018.
  - [37] Yin Li, Xiaodi Hou, Christof Koch, James M Rehg, and Alan L Yuille. The secrets of salient object segmentation. In *Proceedings of the IEEE Conference on Computer Vision and Pattern Recognition*, pages 280–287, 2014.
  - [38] Nian Liu and Junwei Han. Dhsnet: Deep hierarchical saliency network for salient object detection. In *2016 IEEE Conference on Computer Vision and Pattern Recognition (CVPR)*, pages 678–686, 2016.
  - [39] Nian Liu, Junwei Han, and Ming-Hsuan Yang. Picanet: Learning pixel-wise contextual attention for saliency detection. In *Proceedings of the IEEE Conference on Computer Vision and Pattern Recognition*, pages 3089–3098, 2018.
  - [40] Nian Liu, Junwei Han, Dingwen Zhang, Shifeng Wen, and Tianming Liu. Predicting eye fixations using convolutional neural networks. In *Proceedings of the IEEE Conference on Computer Vision and Pattern Recognition*, pages 362–370, 2015.
  - [41] Zhiming Luo, Akshaya Mishra, Andrew Achkar, Justin Eichel, Shaozi Li, and Pierre-Marc Jodoin. Non-local deep features for salient object detection. In *Computer Vision and Pattern Recognition (CVPR), 2017 IEEE Conference on*, pages 6593–6601. IEEE, 2017.
  - [42] Gellért Mátyus, Wenjie Luo, and Raquel Urtasun. Deep-roadmapper: Extracting road topology from aerial images.
  - [43] Roey Mechrez, Eli Shechtman, and Lihi Zelnik-Manor. Saliency driven image manipulation. In *2018 IEEE Winter Conference on Applications of Computer Vision, WACV 2018, Lake Tahoe, NV, USA, March 12-15, 2018*, pages 1368–1376, 2018.
  - [44] Volodymyr Mnih and Geoffrey E Hinton. Learning to detect roads in high-resolution aerial images. In *European Conference on Computer Vision*, pages 210–223. Springer, 2010.
  - [45] Vida Movahedi and James H Elder. Design and perceptual validation of performance measures for salient object segmentation. In *Computer Vision and Pattern Recognition Workshops (CVPRW), 2010 IEEE Computer Society Conference on*, pages 49–56. IEEE, 2010.
  - [46] David Mumford and Jayant Shah. Optimal approximations by piecewise smooth functions and associated variational problems. *Communications on pure and applied mathematics*, 42(5):577–685, 1989.
  - [47] Gattigorla Nagendar, Digvijay Singh, Vineeth N. Balasubramanian, and C. V. Jawahar. Neuro-iou: Learning a surrogate loss for semantic segmentation. In *British Machine Vision Conference 2018, BMVC 2018, Northumbria University, Newcastle, UK, September 3-6, 2018*, page 278, 2018.
  - [48] Stanley Osher and James A Sethian. Fronts propagating with curvature-dependent speed: algorithms based on hamilton-jacobi formulations. *Journal of computational physics*, 79(1):12–49, 1988.
  - [49] Adam Paszke, Sam Gross, Soumith Chintala, Gregory Chanan, Edward Yang, Zachary DeVito, Zeming Lin, Alban Desmaison, Luca Antiga, and Adam Lerer. Automatic differentiation in pytorch. In *NIPS-W*, 2017.
  - [50] Chao Peng, Xiangyu Zhang, Gang Yu, Guiming Luo, and Jian Sun. Large kernel matters improve semantic segmentation by global convolutional network. In *Computer Vision and Pattern Recognition (CVPR), 2017 IEEE Conference on*, pages 1743–1751. IEEE, 2017.
  - [51] Federico Perazzi, Philipp Krähenbühl, Yael Pritch, and Alexander Hornung. Saliency filters: Contrast based filtering for salient region detection. In *Computer Vision and Pattern Recognition (CVPR), 2012 IEEE Conference on*, pages 733–740. IEEE, 2012.
  - [52] Xuebin Qin, Shida He, Camilo Perez Quintero, Abhinav Singh, Masood Dehghan, and Martin Jägersand. Real-time salient closed boundary tracking via line segments perceptual grouping. In *2017 IEEE/RSJ International Conference on Intelligent Robots and Systems, IROS 2017, Vancouver, BC, Canada, September 24-28, 2017*, pages 4284–4289, 2017.
  - [53] Xuebin Qin, Shida He, Xiucheng Yang, Masood Dehghan, Qiming Qin, and Martin Jägersand. Accurate outline extraction of individual building from very high-resolution optical images. *IEEE Geoscience and Remote Sensing Letters*, (99):1–5, 2018.
  - [54] Xuebin Qin, Shida He, Zichen Zhang, Masood Dehghan, and Martin Jägersand. Bylabel: A boundary based semi-automatic image annotation tool. In *2018 IEEE Winter Con-*

- ference on Applications of Computer Vision (WACV), pages 1804–1813. IEEE, 2018.
- [55] Xuebin Qin, Shida He, Zichen Vincent Zhang, Masood Dehghan, and Martin Jägersand. Real-time salient closed boundary tracking using perceptual grouping and shape priors. In *British Machine Vision Conference 2017, BMVC 2017, London, UK, September 4-7, 2017*, 2017.
- [56] Md Atiqur Rahman and Yang Wang. Optimizing intersection-over-union in deep neural networks for image segmentation. In *International Symposium on Visual Computing*, pages 234–244. Springer, 2016.
- [57] Olaf Ronneberger, Philipp Fischer, and Thomas Brox. U-net: Convolutional networks for biomedical image segmentation. In *International Conference on Medical image computing and computer-assisted intervention*, pages 234–241. Springer, 2015.
- [58] Shunta Saito, Takayoshi Yamashita, and Yoshimitsu Aoki. Multiple object extraction from aerial imagery with convolutional neural networks. *Electronic Imaging*, 2016(10):1–9, 2016.
- [59] Karen Simonyan and Andrew Zisserman. Very deep convolutional networks for large-scale image recognition. *arXiv preprint arXiv:1409.1556*, 2014.
- [60] R Sai Srivatsa and R Venkatesh Babu. Salient object detection via objectness measure. In *Image Processing (ICIP), 2015 IEEE International Conference on*, pages 4481–4485. IEEE, 2015.
- [61] Lijun Wang, Huchuan Lu, Xiang Ruan, and Ming-Hsuan Yang. Deep networks for saliency detection via local estimation and global search. In *Proceedings of the IEEE Conference on Computer Vision and Pattern Recognition*, pages 3183–3192, 2015.
- [62] Lijun Wang, Huchuan Lu, Yifan Wang, Mengyang Feng, Dong Wang, Baocai Yin, and Xiang Ruan. Learning to detect salient objects with image-level supervision. In *Proc. IEEE Conf. Comput. Vis. Pattern Recognit.(CVPR)*, pages 136–145, 2017.
- [63] Linzhao Wang, Lijun Wang, Huchuan Lu, Pingping Zhang, and Xiang Ruan. Salient object detection with recurrent fully convolutional networks. *IEEE Transactions on Pattern Analysis and Machine Intelligence*, 2018.
- [64] Tiantian Wang, Ali Borji, Lihe Zhang, Pingping Zhang, and Huchuan Lu. A stagewise refinement model for detecting salient objects in images. In *IEEE International Conference on Computer Vision, ICCV 2017, Venice, Italy, October 22-29, 2017*, pages 4039–4048, 2017.
- [65] Tiantian Wang, Lihe Zhang, Shuo Wang, Huchuan Lu, Gang Yang, Xiang Ruan, and Ali Borji. Detect globally, refine locally: A novel approach to saliency detection. In *Proceedings of the IEEE Conference on Computer Vision and Pattern Recognition*, pages 3127–3135, 2018.
- [66] Zhou Wang, Eero P Simoncelli, and Alan C Bovik. Multi-scale structural similarity for image quality assessment. In *The Thirty-Seventh Asilomar Conference on Signals, Systems & Computers*, 2003, volume 2, pages 1398–1402. Ieee, 2003.
- [67] Saining Xie and Zhuowen Tu. Holistically-nested edge detection. In *Proceedings of the IEEE international conference on computer vision*, pages 1395–1403, 2015.
- [68] Qiong Yan, Li Xu, Jianping Shi, and Jiaya Jia. Hierarchical saliency detection. In *Proceedings of the IEEE Conference on Computer Vision and Pattern Recognition*, pages 1155–1162, 2013.
- [69] Chuan Yang, Lihe Zhang, Huchuan Lu, Xiang Ruan, and Ming-Hsuan Yang. Saliency detection via graph-based manifold ranking. In *Proceedings of the IEEE conference on computer vision and pattern recognition*, pages 3166–3173, 2013.
- [70] Fisher Yu and Vladlen Koltun. Multi-scale context aggregation by dilated convolutions. *arXiv preprint arXiv:1511.07122*, 2015.
- [71] Jianming Zhang, Stan Sclaroff, Zhe Lin, Xiaohui Shen, Brian Price, and Radomir Mech. Minimum barrier salient object detection at 80 fps. In *Proceedings of the IEEE international conference on computer vision*, pages 1404–1412, 2015.
- [72] Lu Zhang, Ju Dai, Huchuan Lu, You He, and Gang Wang. A bi-directional message passing model for salient object detection. In *Proceedings of the IEEE Conference on Computer Vision and Pattern Recognition*, pages 1741–1750, 2018.
- [73] Pingping Zhang, Wei Liu, Huchuan Lu, and Chunhua Shen. Salient object detection by lossless feature reflection. In *Proceedings of the Twenty-Seventh International Joint Conference on Artificial Intelligence, IJCAI 2018, July 13-19, 2018, Stockholm, Sweden.*, pages 1149–1155, 2018.
- [74] Pingping Zhang, Dong Wang, Huchuan Lu, Hongyu Wang, and Xiang Ruan. Amulet: Aggregating multi-level convolutional features for salient object detection. In *IEEE International Conference on Computer Vision, ICCV 2017, Venice, Italy, October 22-29, 2017*, pages 202–211, 2017.
- [75] Pingping Zhang, Dong Wang, Huchuan Lu, Hongyu Wang, and Baocai Yin. Learning uncertain convolutional features for accurate saliency detection. In *IEEE International Conference on Computer Vision, ICCV 2017, Venice, Italy, October 22-29, 2017*, pages 212–221, 2017.
- [76] Xiaoning Zhang, Tiantian Wang, Jinqing Qi, Huchuan Lu, and Gang Wang. Progressive attention guided recurrent network for salient object detection. In *Proceedings of the IEEE Conference on Computer Vision and Pattern Recognition*, pages 714–722, 2018.
- [77] Zhengxin Zhang, Qingjie Liu, and Yunhong Wang. Road extraction by deep residual u-net. *IEEE Geoscience and Remote Sensing Letters*, 2018.
- [78] Kai Zhao, Shanghua Gao, Qibin Hou, Dandan Li, and Ming-Ming Cheng. Optimizing the f-measure for threshold-free salient object detection. *CoRR*, abs/1805.07567, 2018.
- [79] Rui Zhao, Wanli Ouyang, Hongsheng Li, and Xiaogang Wang. Saliency detection by multi-context deep learning. In *Proceedings of the IEEE Conference on Computer Vision and Pattern Recognition*, pages 1265–1274, 2015.
- [80] Wangjiang Zhu, Shuang Liang, Yichen Wei, and Jian Sun. Saliency optimization from robust background detection. In *Proceedings of the IEEE conference on computer vision and pattern recognition*, pages 2814–2821, 2014.